Surfaces and Interfaces 33 (2022) 102257

Contents lists available at ScienceDirect

Surfaces and Interfaces

journal homepage: www.sciencedirect.com/journal/surfaces-and-interfaces

Insights into improved ferroelectric and electrocaloric performance of $Ba_{0.85}Ca_{0.15}Ti_{0.9}Zr_{0.1}O_3$ thick films grown by the electrophoretic deposition

E. Venkata Ramana [a,*], N.V. Prasad [b,*], N.M. Ferreira [a], A. Mahajan [c], I. Bdikin [d], M.A. Valente [a], Fadl A. Essa [e], B. Saleh [f]

[a] Department of Physics, University of Aveiro, I3N-Aveiro, Aveiro 3810-193, Portugal
[b] Materials Research Laboratory, Osmania University, Hyderabad 500 007, India
[c] School of Engineering and Material Science, Queen Mary University of London, London, United Kingdom
[d] Mechanical Engineering Department, Aveiro Institute of Nanotechnology, University of Aveiro, TEMA-NRD, Aveiro 3810-193, Portugal
[e] Mechanical Engineering Department, Faculty of Engineering, Kafrelsheikh University, Kafrelsheikh 33516, Egypt
[f] Mechanical Engineering Department, College of Engineering, Taif University, P.O. Box 11099, Taif 21944, Saudi Arabia

ARTICLE INFO

Keywords:
Electrocaloric
Energy storage
Dynamic scaling
Laser annealing
Electrophoretic deposition

ABSTRACT

Lead-free $Ba_{0.85}Ca_{0.15}Ti_{0.9}Zr_{0.1}O_3$ (BCZT) bulk ceramics have recently gained attention as one of the attractive candidates for electrocaloric cooling due to their large heat absorption capacity induced by electro-structural phase transition near room temperature. However, adiabatic temperature change (ΔT) at room temperature in ceramics has been limited by their relatively low dielectric breakdown strength. Thick films, in this respect, possess the advantages of ceramics (volume) and thin films (thickness). In this work, a systematic ferroelectric and electrocaloric investigation of BCZT thick films, fabricated by electrophoretic deposition combined with laser annealing, has been carried out. Laser annealing at an optimized energy density of 398 W/cm^2 has resulted in densely packed grain morphology with no compositional heterogeneities. Analysis of the scaling behavior of dynamic hysteresis revealed that ferroelectric domain reversal in BCZT/Pt has good stability and low energy consumption in the saturation region. The present thick films exhibited larger breakdown strength of 294 kV/cm and recoverable energy storage density of ~7.3 J/cm^3, at least five-fold enhancement compared to the bulk which is stable up to a 4 mm bending radius. The indirect electrocaloric measurements displayed parameters such as a ΔT and entropy change (ΔS) of 2.94 K and 3.1 J kg^{-1} K^{-1} respectively, for 205 kV/cm which are more than two orders increased compared to the bulk. Higher values of ΔT (1.9 K) at 25 °C, refrigerant capacity of 249 J/kg, and responsivity of 0.143 K mm/kV for BCZT/Pt film compared to relevant lead-free ferroelectric thick films elucidate the potential use of these films for solid-state refrigeration applications. The work also presents electrophoretic deposition with laser annealing as an alternative technique to widely studied tape-casting of thick films for electrocaloric studies.

1. Introduction

The development of lead-free piezoelectrics has gained tremendous attention in the past decade given their various energy conversion applications as sensors, actuators, ultrasonic transducers, resonators, etc. in electronics, aerospace, communications, and medical treatments [1–3]. In this direction, aliovalent doped $BaTiO_3$ (BTO) and solid solutions having morphotropic phase boundary (MPB) were found to show excellent piezoelectric properties [4]. The ceramic composition of 0.5$(Ba_{0.7}Ca_{0.3})TiO_3$-0.5$Ba(Zr_{0.2}Ti_{0.8})O_3$ (BCZT) coined by Liu and Ren has emerged as a material that can be comparable to the $Pb(Zr, Ti)O_3$ (PZT) [5]. Detailed microscopic studies revealed that the emergence of a single-domain state formed due to the field-induced transition to the orthorhombic phase and elastic softening were responsible for unusual piezoelectricity in BCZT [6]. Due to the coexistence of multiple structures in close proximity to room temperature, it is conisidered as one of the primary candidates for electrocaloric studies.

Refrigeration by electric fields based on the electrocaloric effect (ECE) is a promising alternative to the cooling by conventional vapor compression cycle that can curb CO_2 emissions. The ECE of a ferroelectric material is parameterized by changes in temperature (ΔT) and/or entropy (ΔS) induced by polarization state variations with the

* Corresponding authors.
E-mail addresses: venkataramanaesk@rediffmail.com (E.V. Ramana), nvp1969@rediffmail.com (N.V. Prasad).

https://doi.org/10.1016/j.surfin.2022.102257
Received 31 May 2022; Received in revised form 17 July 2022; Accepted 28 July 2022
Available online 2 August 2022

application or removal of an electric field [7]. Achieving and maintaining larger ΔT and ΔS values over a wide temperature range is key for intriguing electrocaloric cooling. PZT or $Pb(Mg,Nb)O_3$ (PMN) - based thin films, ceramics, and multilayer capacitors have exhibited excellent electrocaloric performance with a higher coefficient of performance useful for applications, with a maximum ΔT in the range 1-8 K [8–10]. However, due to environmental hazards posed by the processing of lead-based oxides sustainable lead-free alternatives are in great demand.

BTO-family of piezoelectrics, in this regard, has received prominence due to the coexistence of polymorphic transitions, with a relaxor-like nature, in close proximity which can be tunable to the practical operating temperatures. For example, a large ΔT of 2.4 K was observed for $Ba(Zr_{0.05}Ti_{0.95})O_3$ ceramics at 386 K with first-order phase transition [11]. By driving the BTO into a relaxor-state, $\Delta T > 0.2$ K was maintained over 45 – 60 °C in $Ba(Ti_{0.89}Sn_{0.11})O_3$-$(Ba_{0.7}Ca_{0.3})TiO_3$ solid solution [12]. Similarly, $Ba(Hf_xTi_{1-x})O_3$ exhibited improved ΔT of 1.64 K (117 °C) [13]. However, stronger ECE of ceramics was observed only around phase transitions with poor room temperature ΔT or ΔS values. Thin films or thick films of multilayer ceramic capacitors, on the otherhand, exhibit marked room temperature performance. Thick films of $Ba_{0.95}Ca_{0.05}Ti_{0.94}Sn_{0.06}O_3$ composition were reported to exhibit stronger room temperature ΔT of 1.6 K with improved breakdown strength [14]. One of the significant factors that contribute to improved ECE performance in thick/thin films compared to ceramics has been dielectric breakdown strength originating from the oxygen non-stoichiometry and density subjected to different processing conditions.

Interesting electrocaloric properties have been reported for BCZT ceramics and single crystals [15–18]. Singh *et al.* reported an ECE strength of 0.38 K mm/kV with a ΔT of 0.46 K (131 °C) in 0.55 $(Ba_{0.7}Ca_{0.3})TiO_3$-0.5$Ba(Zr_{0.2}Ti_{0.8})O_3$ single crystals [19]. Sanlialp et al. [20] by direct measurement obtained an ECE strength of 0.165 K cm/kV (65 °C) in BCZT ceramics. In the flux-grown single crystals of BCZT, Liu *et al.* reported extraordinary ECE strength of 1.05 K mm/kV largest ever reported in bulk. ECE in BCZT is quite sensitive to compositional fluctuations relative to that of the MPB. In our previous study, we reported ΔT values of 0.95 - 1.3 K and ECE strength of 0.43 K mm/kV for fiber crystals and ceramics by fine-tuning the chemical composition by laser processing [15]. In ceramics and single crystals, limitations such as maximum applied electric field and geometry limit the ECE strength. Recently, lead-free thick films and multilayers grown by tape-casting were reported to show largely improved electrocaloric performance. Du *et al.* observed a larger room temperature ΔT= 1.6 K at 180 kV/cm for 200 μm thick films of $(Ba_{0.95}Ca_{0.05})(Ti_{0.94}Sn_{0.06})O_3$ fabricated by tape-casting [14]. Ye et al. reported largely enhanced ΔT of -7 K around the phase transition in 12 μm $BaZr_{0.2}Ti_{0.8}O_3$ thick film structure [21]. Zhao et al. found a five-fold enhancement of ECE properties and a larger temperature span of 65 K in 250 μm thick films of potassium-sodium niobate solid solutions compared to their ceramic counterparts [22]. Li et al. found a ΔT = 5.2 K for 13 μm $Ba(Zr_{0.20}Ti_{0.80})O_3$ - $Ba(Sn_{0.11}Ti_{0.89})O_3$ bilayer thick films [23]. However, irrespective of potentiality for refrigeration, there have been no reports on ECE studies of BCZT thick films fabricated by any method. Recently, Barman et al. found a colossal increase in ECE parameters, ΔT = 13.5 K and ΔS = 16.9 J kg^{-1} K^{-1} at 157 °C, in epitaxial BCZT films mediated by larger tetragonal strain [24]. Inspired by the study and considering the advantages of thick films (volume, geometry, and enough material in the active refrigerant compared to thin films) we attempted to study detailed ferroelectric characteristics of BCZT thick films. The stability of polarization states, energy dissipation within one period of domain reversal, and ECE properties of BCZT thick films have been investigated.

The thick film approach is also known to be the low-cost approach for micron-sized films that can have the advantages of ceramics and thin films that can facilitate intermediate breakdown strength. Electrophoretic deposition (EPD) is one such method that uses powder technology to produce uniform thick films on metal. In this method, deposition occurs when the electric field-driven colloidal particles of fluid suspension migrate towards the electrode of the liquid-liquid interface [25]. EPD has maintained its relevance as an industrial as well as academically scalable technique for multiple applications. However, the finished product, post-annealing, endures a high degree of porosity which is detrimental to ECE.

In our previous work, we reported on the optimization of growth parameters for uniform deposition of thick films and the effect of laser power & exposure time on microstructure as well as local domain switching measured by the piezoresponse force microscope [26]. The present work is aimed to study the detailed ferroelectric and electrocaloric properties of BCZT thick films, obtained by the combination of EPD growth and laser annealing, as a function of temperature. The work also presents a key kinetic picture of domain reversal by dynamic scaling behavior of BCZT/Pt film in comparison with the literature on BTO-based materials. We found improved room temperature ECE and refrigerant capacity of thick films relative to ceramics.

2. Experimental

BCZT thick films were fabricated by the EPD process using powder particles processed by the ceramic method, reported elsewhere [27]. For this, high purity (99.9%) stoichiometric reagents $BaCO_3$, $CaCO_3$, TiO_2, and ZrO_2 were ball milled for 18 h in an ethanol medium with a speed of 500 rpm (Retzsch, GmbH). The resulting slurries were dried and calcined twice at 1300 °C for 4 h. The powder was then milled again for 24 h and sieved to 1-micron size. The particle size of 0.55 μm (Fig. S1 a) was estimated using the particle size analyzer (Mastersizer 3000, Malvern Panalytical). A highly stable suspension of particles in acetone (0.70 g/100 ml.) was obtained and thick films were deposited on Pt foil by applying a voltage of 60 V for 2 min. The zeta potential of the powder suspension (pH=9) was measured to be 31 mV. The electrode surface area was 1.2 cm^2 and the working distance between the opposite platinum electrodes (Fig. 1a) was kept at 20 mm during the deposition. A detailed description of stable suspension preparation and the EPD deposition process was presented in our previous work [26].

Wet films, thus obtained, were dried in the oven at 60 °C for 24 h. BCZT films were subjected to raster scanning of the chosen area of the film using the continuous CO_2 SLC laser (GSI Spectron, $\lambda = 10.6$ μm) [15, 26,28] with a spot size of 4 mm. The laser beam was focused over the target area of 5 mm x 5 mm and mounted on an X-Y stage where the scanning speed was optimized to be 0.1 mm/s. The laser power was optimized to be 50 W which corresponds to the laser power density of ~398 W/cm^2 (we arrived at this conclusion after initial annealing experiments under 199 – 597 W for 5 – 30 min.). The schematic of laser annealing of BCZT thick films is presented in Fig. 1(b). For the comparison of different structural properties, ceramic samples were prepared from the BCZT powder: it is mixed with a 2% polyvinyl alcohol (PVA) binder, pressed into discs of 7 mm diameter, and sintered at 1520 °C for 4 h.

Structural studies of thick film samples were carried out by grazing incidence (0.5°) X-ray diffraction (GIXRD, XPert-PRO diffractometer, equipped with graphite monochromated Cu K_α radiation. Surface and cross-sectional microstructure, and elemental mapping were carried out by a scanning electron microscope (SEM, Hitachi SU70) equipped with energy-dispersive X-ray spectroscopy (EDS). The grain size was analyzed using the Image J software. The film thickness was measured using a step profiler (Dektak 150, Veeco). Chemical composition was also assessed from the electron probe microanalysis (EPMA) measured by field emission SEM (Zeiss Gemini 2 with wavelength dispersive spectroscopy, WDS, detector, Oxford instruments) with prior calibration of 211 × 285 mm area using a standard basis for different chemical elements (with ref. 9877 from Micro-Analysis Consultant Ltd) [29].

To study electrical properties by capacitor geometry, square-shaped Au top electrodes (300 × 300 μm) were deposited using DC sputtering and a shadow metal mask. Temperature (from -150 to 200 °C) dependent dielectric measurements were carried out in the frequency range

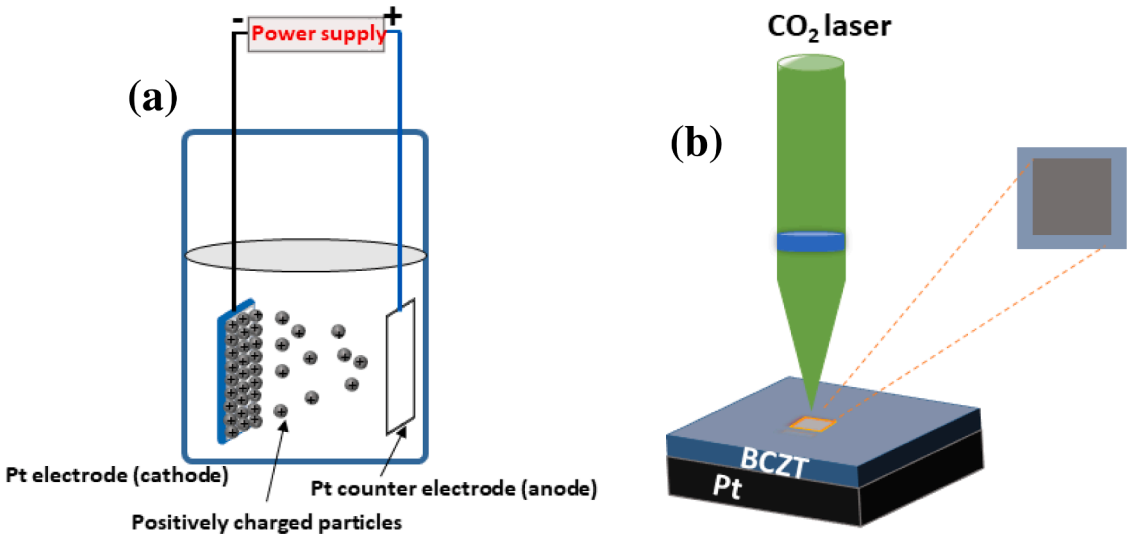

Fig. 1. Processing of BCZT thick films. (a) Schematic representation of electrophoretic deposition of powder particles. (b) Laser annealing of thick film using the continuous laser beam with a scanning speed of 0.1 mm/s.

100–10^6 Hz using an impedance analyzer (Agilent 4294A). Polarization-electric field ($P-E$) hysteresis loops were measured using the hysteresis loop tracer TF-Analyzer (aixACCT) at different frequencies in the range 0.5–12 kHz. Loops were also measured as a function of temperature up to 190 °C with a step size of 5 °C. The electrocaloric performance of BCZT/Pt films was assessed based on the P-E-T relations. Local piezoresponse (PFM) measurements were carried out using a commercial atomic force microscope (Veeco AFM Multimode Nanoscope-IV MMAFM-2). For PFM imaging, phosphorus-doped Si cantilevers with the resistivity 0.01−0.02 Ω-cm and tip apex radius less than 10 nm with spring constant = 7.4 N/m were used (Nanosensors). AC voltage of 5 V at a frequency of 35 kHz was applied. Experimental details of structural and electrical characterization are presented in the supplementary.

3. Results and discussion

Fig. 2(a) presents GIXRD analysis of laser annealed BCZT/Pt film in comparison to the as-grown film and ceramic with optimized composition as well as sintering temperature. BCZT film exhibits all the perovskite peaks, with no preferential orientation, which can be indexed

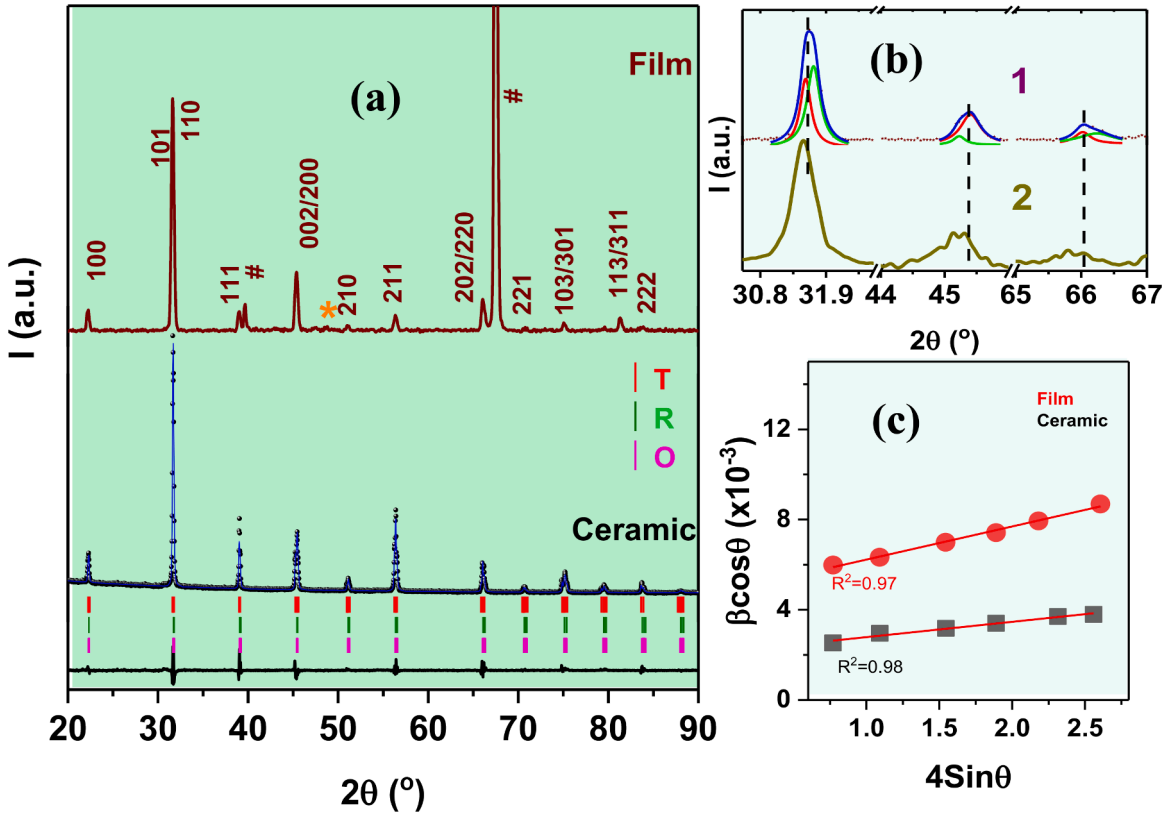

Fig. 2. (a) Grazing incidence X-ray diffraction of BCZT/Pt thick film. XRD data of ceramic is also presented for reference. (b) GIXRD with fittings of BCZT/Pt film after laser annealing (1) compared to the as-grown film (2). (c) Williamson-Hall plots for the film and ceramic.

based on different polymorphs of BTO with a dominant tetragonal phase (*P4mm*). It was observed that 2θ positions of laser annealed film shifted towards the higher angle side compared to as-grown and ceramic samples indicating material-laser interactions. The presence of peaks corresponding to Pt and BCZT indicates that laser annealing has possibly resulted in the grain growth of the expected phase during the laser-solid reaction. A small (~1%) minor peak (*), merged in the background, observed around 2θ=48° can be due to the presence of $BaTi_2O_5$.

In order to understand the contribution of different BTO-based crystalline phases of the BCZT precursor and to estimate lattice parameters, we performed Rietveld refinements, to the powder XRD of ceramic, using the GSAS software. The resulting graphic output is presented in Fig. 2(a) while the fitting analysis and agreement factors along with the phase compositions are presented in Table S1. The inclusion of tetragonal (T), rhombohedral (R, *R3m*), and orthorhombic (O, *Amm2*) in the refinement step has resulted in the best fits with R_P =9.17%, R_{WP} =4.11%, and χ^2 =3.78. The phase composition of the T, R, and O phases were estimated to be 57.8%, 13.3%, and 28.9%, respectively. This phase distribution agrees well with the literature on BCZT ceramics with optimized piezoelectric properties (T: R: O as 56: 32: 12) [15,30].

The annealed thick film, however, exhibited broader peaks with the clear splitting of peaks around $2\theta = 31$, 45, and 66 ° that could be fitted with the Lorentzian function. A detailed image is presented in Fig. 2(b) where changes in as-grown and annealed films were also shown. These features correspond to the morphotropic phase boundary of BCZT nominal composition and signify no major alterations to the crystallographic phases. Unit cell parameters calculated for the film were a = 3.962±0.007 and c =3.978±0.003 Å in comparison to the bulk (a = 4.007, c = 4.025 Å) [5]. The difference in lattice parameters indicates a significant lattice strain due to different thermal expansions of dissimilar materials (Pt and ceramic BCZT). It can also be seen that the BCZT film experiences a compressive in-plane strain of ~ -1%. This can be due to the lattice mismatch of 1.7% (between BCZT & Pt) and different thermal expansion coefficients (CTE). Considering the CTE_{BTO}=5.3 and 7.5 ppm/K for O and T phases, respectively [31] and CTE of cubic Pt ~ 9 ppm/K, it is likely that a significant in-plane compressive stress develops in the BCZT films on Pt foil, during the laser annealing and rapid cooling processes. These strains are expected to alter the polarization behavior of the film significantly, as observed in previous studies of ferroelectrics on metal foils [32,33].

The effect of laser annealing and subsequent changes to BCZT lattice have been analyzed from the thin film strain calculations in comparison

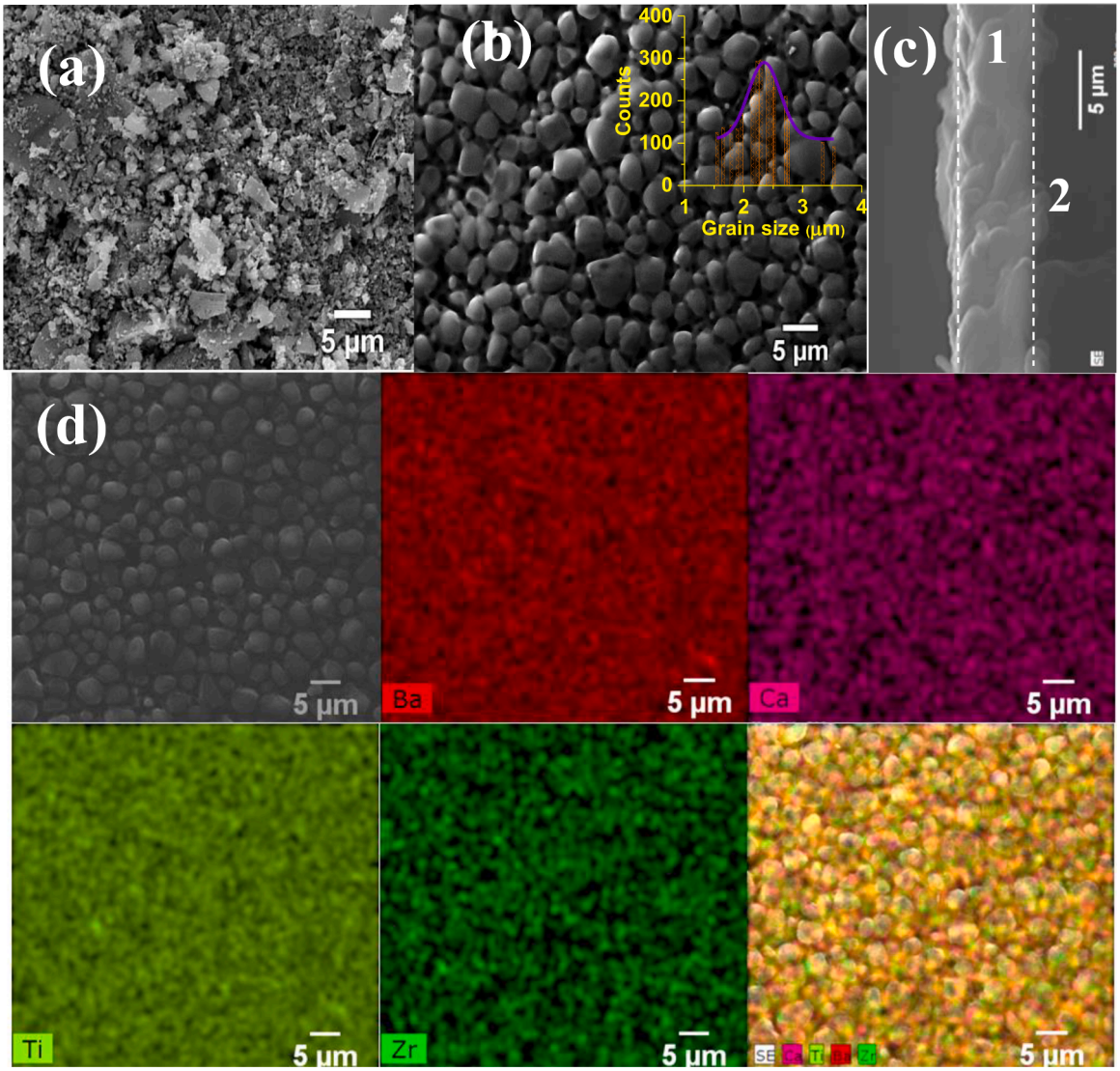

Fig. 3. Scanning electron micrographs of BCZT thick film. Surface morphology of (a) as grown BCZT/Pt film, (b) laser annealed BCZT/Pt film with densely packed grain microstructure and (c) cross-sectional SEM image that represents typical film thickness. Numbers 1 and 2 represent the film BCZT and substrate Pt. (d) SEM-EDS compositional map of BCZT/Pt film.

to the free-standing case (ceramic). The peak broadening observed in thick films can be due to factors such as finite thickness induced inhomogeneous strain and the instrumental resolution of the diffractometer. The latter has been taken care of by means of calibration using a reference single crystal while the former is estimated by looking at the peak width for different reflections and fitting the results using a Williamson-Hall (W-H) relation [34] given by $\beta_{hkl}\cos\theta = \frac{K\lambda}{D} + 4\epsilon\sin\theta$ where λ is the x-ray wavelength (1.54056 Å), K is the geometric constant equal to 0.91, D is the coherence length along the scattering vector, perpendicular to the thin film surface, β_{hkl} is measured peak width at half-maximum intensity (FWHM), ε is the microstrain and θ is the X-ray angle. The inhomogeneous strain has been extracted from the slope of the linear fit of $\beta\cos\theta$ *vs.* 4sinθ plot (Fig. 2c). The ε values for BCZT film and ceramic are 0.15% and 0.068% respectively. The film exhibits a larger microstrain compared to the relaxed state (ceramic). In addition to the rapid annealing process, the microstrain could also be created due to lattice distortion as a result of surface clamping effects that are reflected as the broader peak. This analysis is plausible considering that the BCZT film on the Pt substrate is polycrystalline and has no preferred orientation, similar to the W-H analysis reported for polycrystalline (Ba, Sr)TiO_3 films on stainless-steel substrate [35].

General grain morphology of the precursor BCZT powder, as-grown and laser annealed BCZT films are presented in Fig. S1 (a), Fig. 3(a) and Fig. (3b, S1 b) respectively, measured by the SEM. Densely packed grain structure with well-defined boundaries can be seen due to laser annealing, which, otherwise results in higher porosity when the films are thermally treated in a conventional furnace for 1400 °C for 2 h. The laser irradiation of 15 min. was enough to transform the green bodies into well-densified films with no visible liquid phase. The average grain size of the film, estimated from the statistics of histograms (inset of Fig. 3b), was 2.35 μm. When the films were laser annealed at higher power densities (>500 W/cm^2) larger grains with needle-like interstitials were observed which is caused by the excess liquid phase. The SEM image of thick film annealed at 598 W/cm^2 is presented in Fig. S1 (c) in comparison to the optimized condition. The morphological differences observed in the films of optimized conditions and higher laser power are attributed to additional phases and compositional heterogeneities. During the laser annealing when the incident photon energy ($h\nu$) is higher than the material's bandgap (E_g), the surface absorbs the radiation effectively (Tauc's relation). Since the BCZT is semi-transparent to visible light ($E_g > 3.5$ eV), the laser energy is absorbed by the surface of the film and heated up indirectly due to thermal diffusion. By the choice of laser and exposure time, the penetration depth can be tuned to the film thickness. The cross-sectional SEM image (Fig. 3c) presents a clean metal-thin film interface indicating adequate penetration of laser irradiation with no damage to the substrate. The average thickness of the processed film of Fig. 3b was found to be 4.3 μm. SEM-EDS images measured on the surface of BCZT/Pt thick film (Fig. 3d) display the presence of expected elements that are distributed uniformly across all the grains of measured area. A detailed quantitative analysis of different

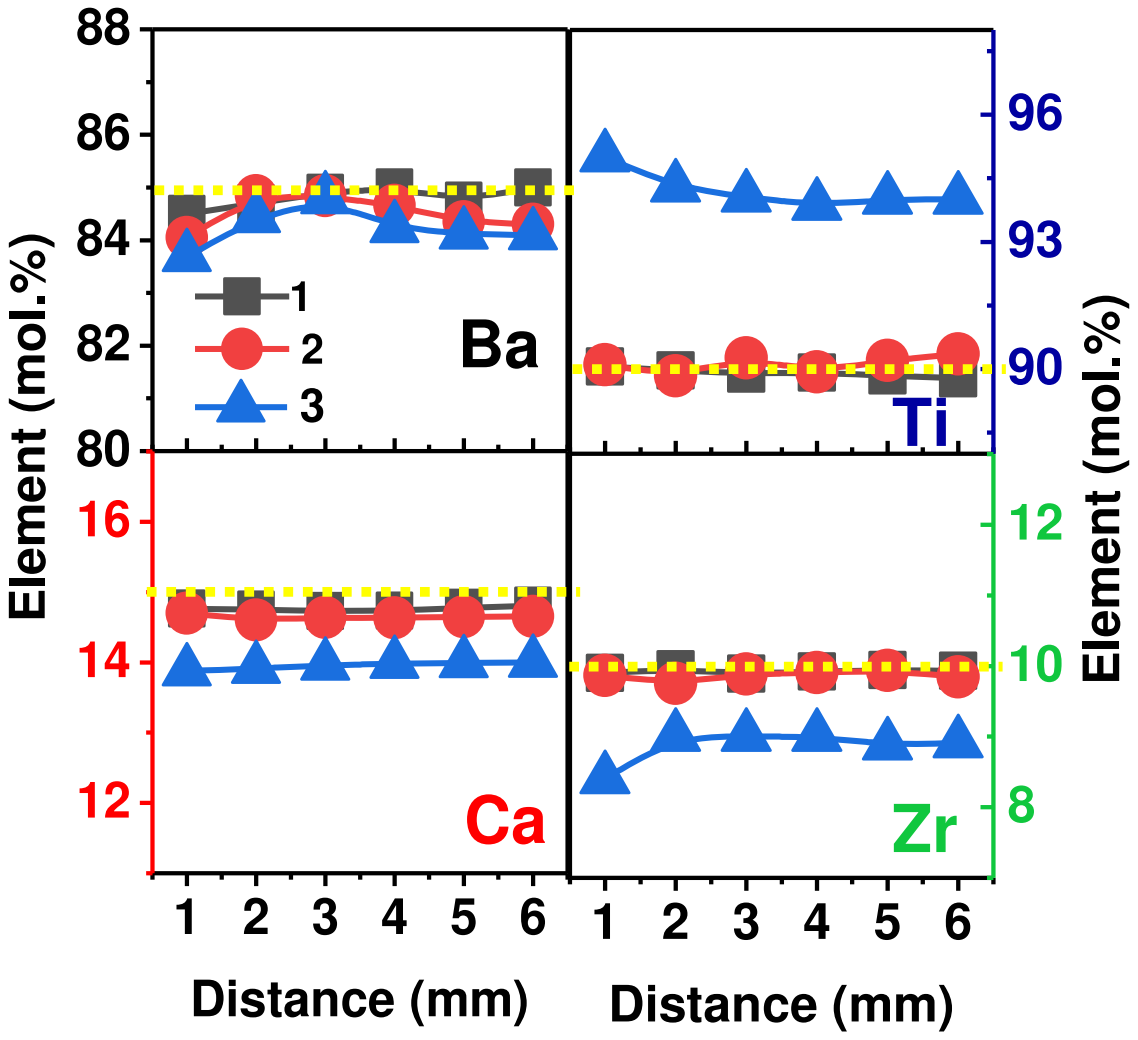

Fig. 4. EPMA estimated compositional percentage of elements (in mol.) measured for as-grown (1), annealed at optimized (2), and higher (3) laser energy density (598 W/cm2). Here horizontal dotted lines (yellow) represent expected mol.%.

elements is presented below.

The chemical composition of the laser annealed film was estimated from the EPMA measurements. The area scans were performed on different regions of the film and Ba, Ca, Ti, Zr, and O were estimated by scanning reference targets BaF_2, CaF_2, Ti-metal, Zr-metal, and MgO respectively. In our recent studies, we found that BCZT solid-laser interactions can cause heterogeneity in different cations, especially the Zr, based on the laser energy and exposure times [15,26]. Fig. 4 presents the estimated composition (symbols) with reference to the expected cationic percentages (lines) of three different films: as-grown (1), optimized (2), and higher laser power density (3). The results indicate that the optimized laser energy density maintained the cationic ratios of the MPB composition while the one annealed at higher power presented compositional heterogeneities with excess Ti and Zr-deficient regions. Based on this observation we chose the optimized BCZT thick film for electrical characterization.

Fig. 5(a) presents the polarization switching characteristics of BCZT films as a function of electric field (E_0) at a fixed frequency. *P-E* loops measured at 500 Hz exhibit saturation behavior within the E_0 range of 0–205 kV/cm. The remanent polarization (P_r), polarization maximum (P_{max}), and coercive field *vs.* E_0 plots (Fig. 5b) demonstrate that the laser annealed film has soft ferroelectric nature, conforming to bulk BCZT. The P_r and E_C values of 14 μC/cm^2 and 13.5 kV/cm respectively, are distinct from BCZT films grown by chemical or physical techniques where the coercivity is larger arising from nanometre-sized grains [36,37]. Moreover, improved polarization maximum and lower E_C compared to thin films stems from the easier domain rotation due to the lower number of domain walls in micrometer-sized grains. Thus the present ceramic films possess unique advantages of ceramics and thin films that can withstand up to larger electric fields. The polarization current exhibits maxima during positive and negative field drives indicating 180 ° domain reversal. The observation of peak splitting in I_P can be due to the existence of polar nanoregions (PNRs) due to relaxor-like ferroelectric order which is also the case for single-crystalline BCZT fiber crystals reported by us recently, due to inhomogeneous cationic ratios that occur in the mixture of Zr- and Ti-rich matrices [15]. However, in the present case, the thick film sample does not show such compositional heterogeneities. From the analysis of temperature-dependent permittivity of BCZT/Pt film, we observed that the phase transition was diffused (T_m at 103 °C), accompanied by no significant dispersion in T_m with frequency, and the degree of diffusivity (γ) was 1.84 (Fig. S2). Relaxor-like behavior of BCZT has been observed previously in epitaxial and polycrystalline thin films grown by the PLD [24,37,38]. In contrast to thin films of nanometre-sized grains, the physical properties of laser annealed films can be compared to the thick films derived by tape-casting or screen printing due to the microstructural correlations. Improved P_{max} of 38 μC/cm^2 compared to the bulk is identical to the few micron-sized BCZT film processed by the screen-printing on Pt/Si substrate, where P_{max} and P_r were reported to be 35 and 22 μC/cm^2 respectively for a loop which is relatively "fat" [39]. BCZT thick films produced by the tape-casting technique were reported to possess P_{max} and P_r of 17 and 8 μC/cm^2 respectively [40]. However, compared to the above film processing techniques that involve longer heat treatment protocols and related porosity, unfavorable to the polarization for electronic applications, the optimized laser treatment is beneficial in terms of time as well as larger areas.

To understand the stability of domain switching against external electric fields in our insulator/metal thin films, P-E loops under various E_0 and frequencies were analyzed. The polarization reversal is a dynamic process of domain walls and is closely related to the frequency at which E_0 is applied. Fig. 5(c) demonstrates pronounced changes to the P-E loop at different fixed frequencies in the range 0.5-12 kHz at a maximum E_0=205 kV/cm: (1) there has been a negative correlation between the P_{max} (or P_r) and the measuring f and (2) the E_C gets significantly larger. At the same time, the hysteresis area also shows a progressive but monotonous decrease with the frequency. To find the correlation between polarization and electric field dynamic hysteresis analysis has been performed: area under the ferroelectric loop <A>, E_0 and f are related by the power-law relation $\langle A\rangle \propto f^m E_0^n$ where the parameters m and n are controlled by domain states and polarization

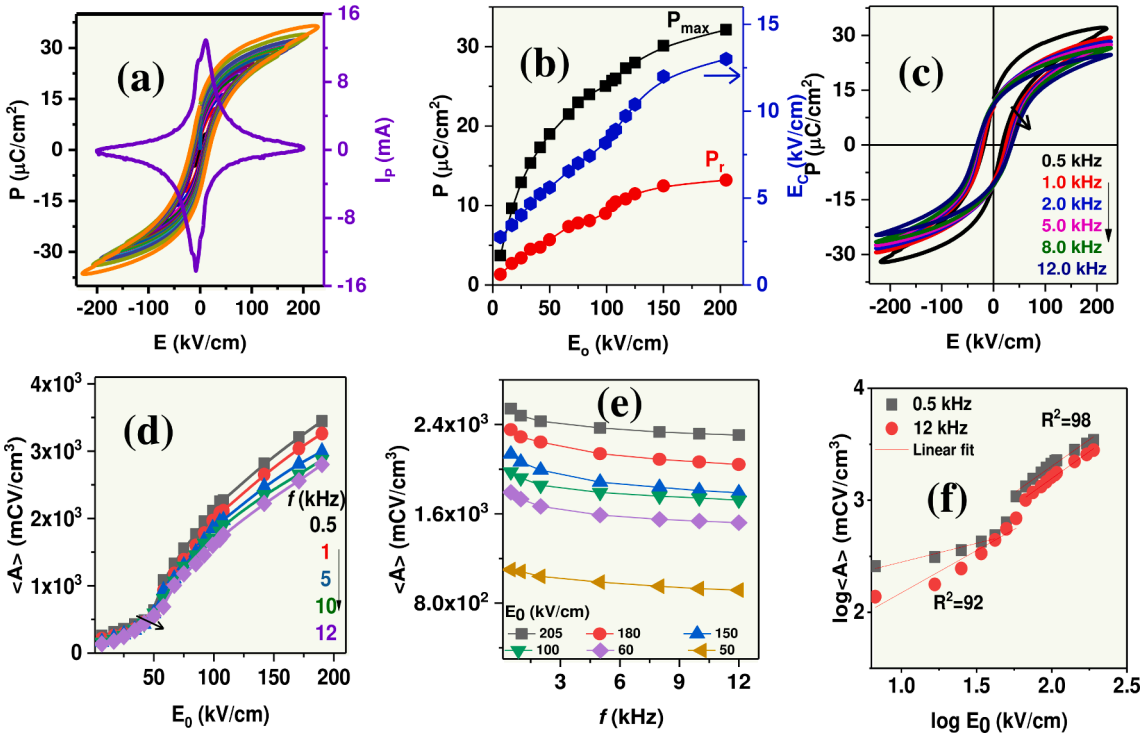

Fig. 5. Room temperature polarization - electric field hysteresis loops of BCZT/Pt thick film: (a) P-E relation under different E0 and IP at E0 max measured at 500 Hz. (b) E0 vs. Pmax, Pr, and EC. (c) frequency dependence of polarization at E0 max. (d) Variation of hysteresis loop area as a function of E0 at different fixed frequencies. (e) <A> vs frequency at fixed E0. (f) The relationship between log<A> and logE0 measured at fixed frequencies, 0.5 and 12 kHz.

switching characteristics [41,42]. This relation indirectly reflects the kinetic behavior of domains such as nucleation, growth, their motion, and the corresponding polarization reversal process. Power-law exponents m and n refer to the switching time required by domains at a specific E_0 and the ability of domains by which they respond to changes in E_0 direction, respectively. The value of m is considered to be a function of charge defects and space charges and its higher negative value represents higher domain switching time. Similarly, a higher n means sharper response and higher polarization.

Fig. 5(d) presents the relation between the E_0 and <A> at different fixed f which shows an increasing trend of the area with the applied field though the increase is distinct at different E_0 ranges: 20-60 kV/cm ($4E_C$) and up to 205 kV/cm. Similarly, the hysteresis area was found to decrease with the increase in f at different fixed E_0. The power-law coefficients m and n were calculated from the relations $\langle A\rangle \propto f^m$ and $\langle A\rangle \propto E_0^n$. From Fig. 5(d) and 5(f) it is evident that the loop area at a fixed f rises rapidly in the range of 20 – 60 kV/cm (sub-saturated field) and then slowly in the saturated region (70–205 kV/cm). It is understood that the domain reversal occurs mainly below 70 kV/cm ($E_0 \geq 4E_C$) where the energy dissipation increases rapidly, resulting in the raise in <A>. It is noteworthy that BCZT at room temperature is relaxor-like, the switching of 180° domains and the reorientation of PNRs oriented parallel towards E_0 is also expected. With the increase in electric field in the range sub-saturated to saturated region, the reorientation of nanodomains or PNRs would facilitate the polarization rotation of the nearby domains [43]. Similar results were also found in other relaxor-like ceramic 94% $(Bi_{0.5}Na_{0.5})TiO_3$-6%$BaTiO_3$ [42], PMN-PT [44,45] and $BaTiO_3$ ceramic [46] at 25 °C where 2 (or 3)-stage scaling behavior was observed. With further increase in E_0 towards saturation results in lower n, as the majority of domains are already reversed, leaving a few domains which have either difficulty in reversal or pinned. In this way, newly added reversed domains are smaller and the growth of <A> slows down. For instance, in this stage, since the E_0 is large enough to switch all 180° domains the reduced rate of increase in <A> mainly results from the continuous rotation of activated non-180° domains toward the field direction, similar to the behaviour observed in $(Na_{0.5}Bi_{0.5})TiO_3$-based relaxor ceramic [47].

Frequency-dependent scaling relationship obtained at different fixed E_0 values is presented in Fig. 5(e). The hysteresis area was found to decrease gradually with increasing frequency and log<A> *vs.* log f follows a linear relation. When f increases from 0.5 to 12 kHz, <A> decreases by ~22% and 10-12% for sub-saturated fields (60 kV/cm) and saturated fields respectively. The change in <A> is controlled by the competition between the period of electric field ($1/f$) and the characteristic time period (τ) taken to complete the domain reversal. The τ is expressed as $\tau \propto \sqrt{\tau_n \times \tau_g}$, $\tau_n = 1/\nu_n$, $\tau_g = 1/\nu_g$ where ν_n is the domain nucleation rate, ν_g is the domain boundary growth velocity. At lower frequencies ($1/f > \tau$), domains can reverse under lower fields in enough time and consume less energy. Furthermore, when the period of $E_0 < \tau$, the domain reversal cannot catch up with the variation in E_0 consequently the <A> or the consumed energy by domain reversal in each cycle of the field decreases with the increase in f. It is observed in this study that when the E_0 was around 60 kV/cm, there has been a higher slope change (in log<A> vs log f plot) and at higher E_0, near saturation, the slope change decreases by half. A higher electric field is required for domain switching at high frequencies than at lower frequencies resulting in the increased E_C.

The evolution of <A> with respect to E_0 and f can thus be scaled to relations: $< A > \propto f^{-0.07}E^{1.7}$ in the sub-saturation region and $< A > \propto f^{-0.04}E^{1.1}$ in the saturated region. From the temperature-dependent dynamic scaling study, values of exponents m and n for BTO were reported to be different for different structures: -0.16 & 3.04, -0.28 & 3.04 (-0.16 & 1.38), -0.3 & 3.49 (-0.28 & 0.86) for R, O and T phases in the sub-saturation (saturation) regions, respectively [46]. Hence, the values of m and n are thus related to the symmetry and dimensional changes of a given ferroelectric. It can be inferred here that the absolute value of m refers to better stability of domain reversal around the frequency of the experiment. The coexistence of R, O & T at room temperature and thick film microstrain have resulted in different scaling behaviour, typical to the MPB composition of BCZT. At the same time, the lower value of exponent n for BCZT/Pt suggests that the domain reversal consumes less energy under higher electric fields, compared to classical BTO.

The energy storage performance of BCZT/Pt thick films is described in Fig. 6(a). From the P-E loop measured at 1 kHz, the energy density was calculated using the following relations: $W_{tot} = \int_0^{P_m} EdP$, $W_r = \int_{P_r}^{P_m} EdP$, $\eta = \frac{W_r}{W_{tot}}$. Here, W_{tot}, W_r and η corresponds to total energy density, the recoverable energy density, and the efficiency of the dielectric capacitor. The film exhibits W_r and η values of ~7.3 J/cm^3 and 75%, respectively compared to 0.7 J/cm^3 and 71% observed for BCZT ceramic

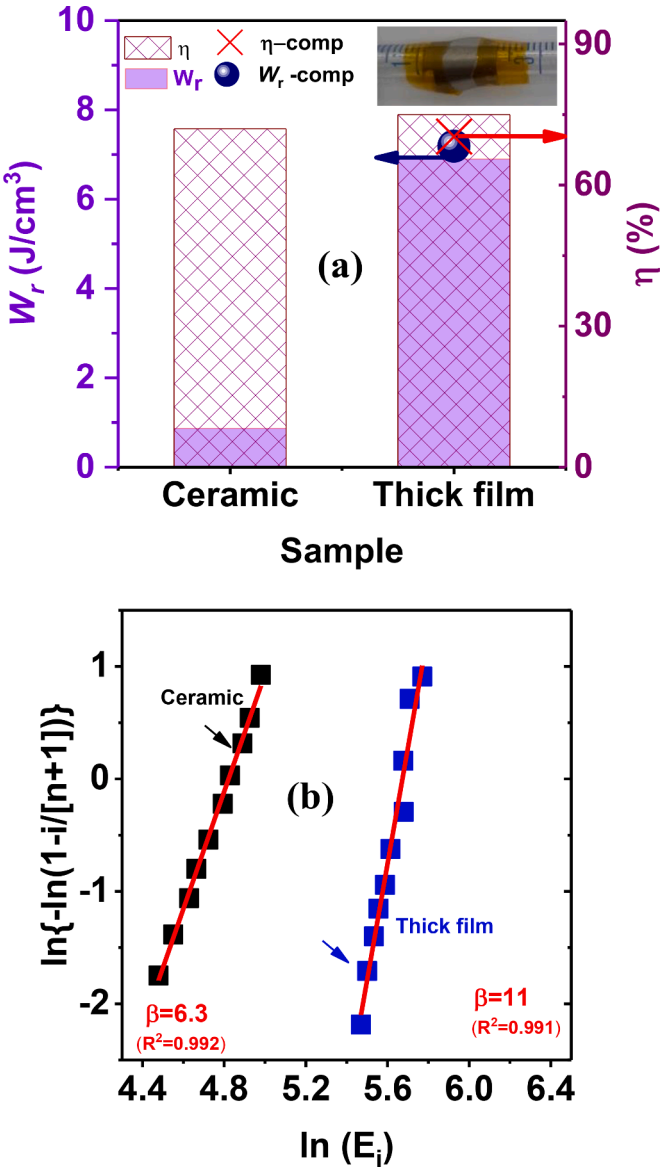

Fig. 6. (a) Energy storage characteristics of BCZT/Pt film. Symbols represent storage parameters under compression. Insert: image of the thick film in the compressed state with a 4 mm bending radius. (b) Weibull distribution plots of the breakdown strength of BCZT thick film and ceramic.

[15]. These values are on the lower side compared to nano-grained BCZT thin films [48] and at the same time marked enhancement compared to ceramics, which is the feature of thick films of EPD growth or tape-caste layers. The integration of ferroelectric ceramic with the metal as a thick film has facilitated the enhancement of maximum E_0 that can be applied for driving the ceramic into a saturation state. Additionally, owing to thick films' flexibility, energy density measurements were conducted up to a bending radius of 4 mm (compressed state, inset of Fig. 6a), and no significant difference in W_r values was observed within the experimental error range.

The breakdown strength (BDS) is an important parameter for the energy storage performance of the dielectric capacitors since the storage density is strongly dependent on the maximum applied electric field. To determine the BDS of present samples widely employed two-parameter Weibull distribution has been employed which is governed by the following expressions:

$$P = 1 - exp\left[-\left(\frac{E_i}{E_b}\right)^{\beta}\right],$$

$$X_i = \ln(E_i),$$

$$Y_i = \ln\left(\ln(1-P_i)^{-1}\right),$$

$$P_i = \frac{i}{n+1}$$

The symbols P/P_i, E_i, n, i, E_b, and β represent the breakdown probability of the sample, breakdown strength of capacitor i in a series of n (n = 8 – 10) devices of the same type (E_1, E_2..E_n), mean BDS, and shape parameter respectively. -β$\ln E_b$ is equal to the intercept that signifies the magnitude of BDS. From the linear fitting of Y_i vs X_i, the BDS, as well as ß of BCZT samples (thick film & ceramic), are calculated and the results are presented in Fig. 6(b).

The breakdown strength values, extracted from the intercept of line with the line Y=0, for thick film and ceramics were found to be 294 kV/cm and 140 kV/cm respectively. At the same time, the values of $\beta > 6$ for ceramic and thick films indicate reliable fitting of Weibull distribution. The BDS values observed in BCZT films should be the characteristic pertinent to thick films on account of the grain size, porosity, geometry (BDS increases exponentially with the decrease in thickness), and composition, in conjunction with the literature on thick films grown by tape casting [49]. The BDS of 140 kV/cm for the ceramic sample is comparable to BCZT ceramics observed in literature having high density and precisely controlled composition: 118 kV/cm for pristine BCZT, Sm-doped BCZT [50], 140 kV/cm for 0.1BCT-0.9BZT [51]. The improved quality of BCZT thick films subjected to the rapid annealing process by the laser also contributes significantly to the improved storage performance since the EPD grown thick films with conventional

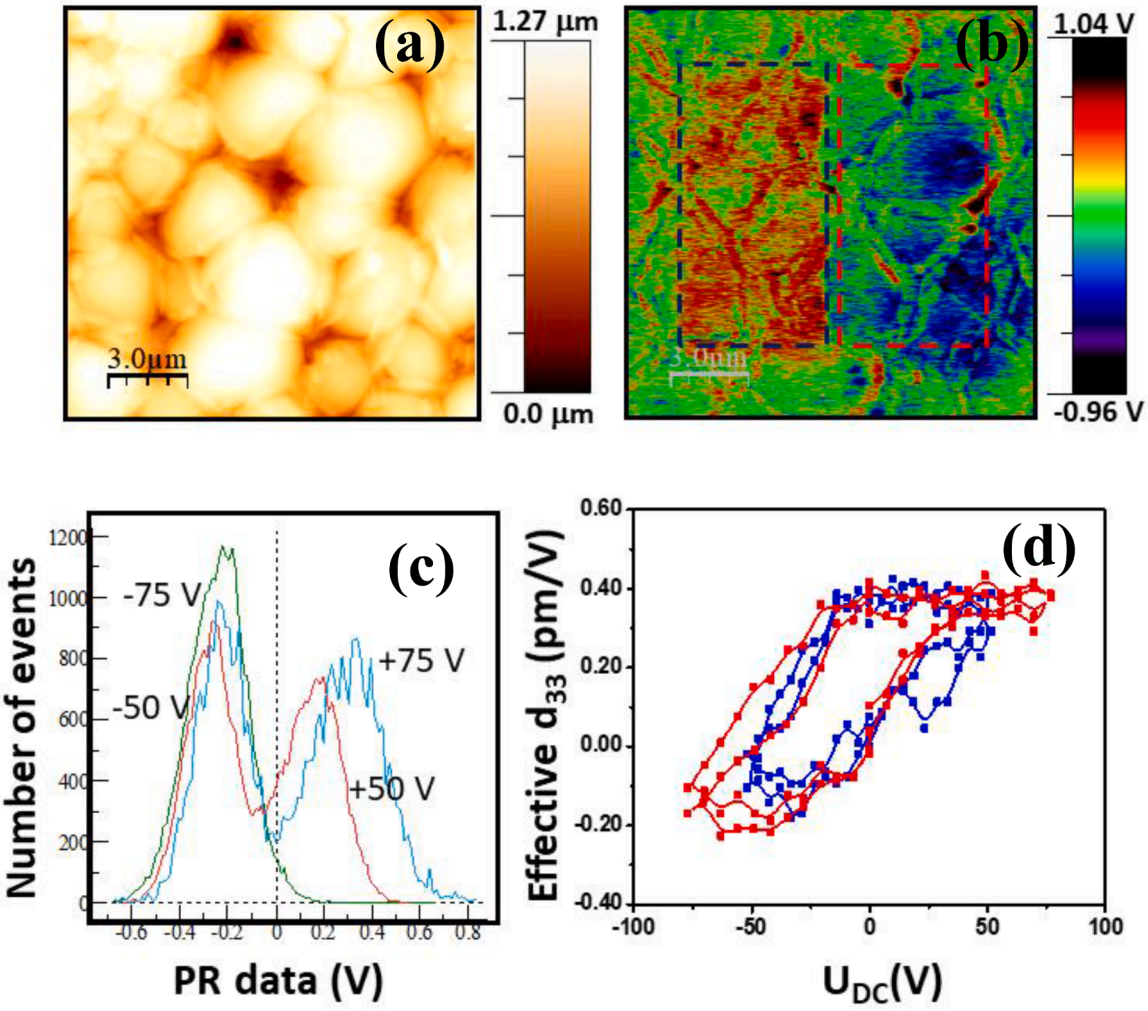

Fig. 7. Piezoresponse force microscopic results of the optimized BCZT/Pt thick film. (a) Surface topography, (b) vertical (out-of-plane) piezoresponse and poling results (under +75 & -75 V). (c) Piezoresponse comparison under 50 (red) and 75 V (blue), green is original. (d) Local PFM hysteresis loops.

sintering typically results in porosity [52].

Local piezoresponse (PR) of BCZT thick films on Pt foil was assessed with the help of an atomic force microscope operating in PFM mode. Fig. 7(a), topography, describes the grain morphology pertinent to laser annealing under optimized conditions that encompasses a rough surface (root mean square roughness of 50 nm) and grain size of 2.4 μm, on average. Lateral and vertical PFM responses were measured to understand periodic changes in polarization of observed ferroelectric grains. The presence of polar domains with boundaries has been evidenced by the vertical piezoresponse image (Fig. 7b) which also illustrates the morphological relation. Given the inherent rough surface of the thick film, the cross-talk of the piezoresponse to morphological features can be a possibility. Predominantly out-of-plane polarization and a weaker lateral PFM response (not shown) observed in this sample can be due to lower d_{15}. Domain reversal has been studied by local poling experiments which revealed a strong imprint of positive and negative bias. Increased piezoresponse after poling at different fields can also be found in the PR profiles (Fig. 7c,d). Local hysteresis loops further describe the switchable polar domains for voltages under 100 V. The observation of broader loops indicates the influence of a stronger inner depolarization field and screening potential from the neighbouring domains. In addition, asymmetric d_{33} loops can also be due to metallic substrate due to the different work functions. However, this can be neglected on account of Pt coated tip as a top electrode and Pt bottom electrode during the measurement. According to the literature, a delocalized built-in field that arises from the inequivalent interfaces of the ferroelectric layer, and the localized fields arising from charged defects inherent to the ferroelectric contribute to the asymmetry in local hysteresis loops [53,54]. The effects of internal fields are noticeable under the electrostatic field of a sharp metal probe in the nanoscale volume under the probe compared to bulk polarization which is a collective effect of domain nucleation and domain wall motion. The PFM response of thick films under higher laser power (Fig. S3) exhibited fibrous grains with isolated domains, completely different from the optimized one. The results indicate that BCZT/Pt film exhibited inherent polarization with a strong correlation to annealing conditions, distinct from the stronger PFM response observed for BCZT ceramics [15].

To evaluate the electrocaloric response of BCZT thick film, temperature dependent hysteresis loops of 1 kHz were recorded in the range of 18–190 °C with an interval of 5 °C and the results are displayed in Fig. 8.

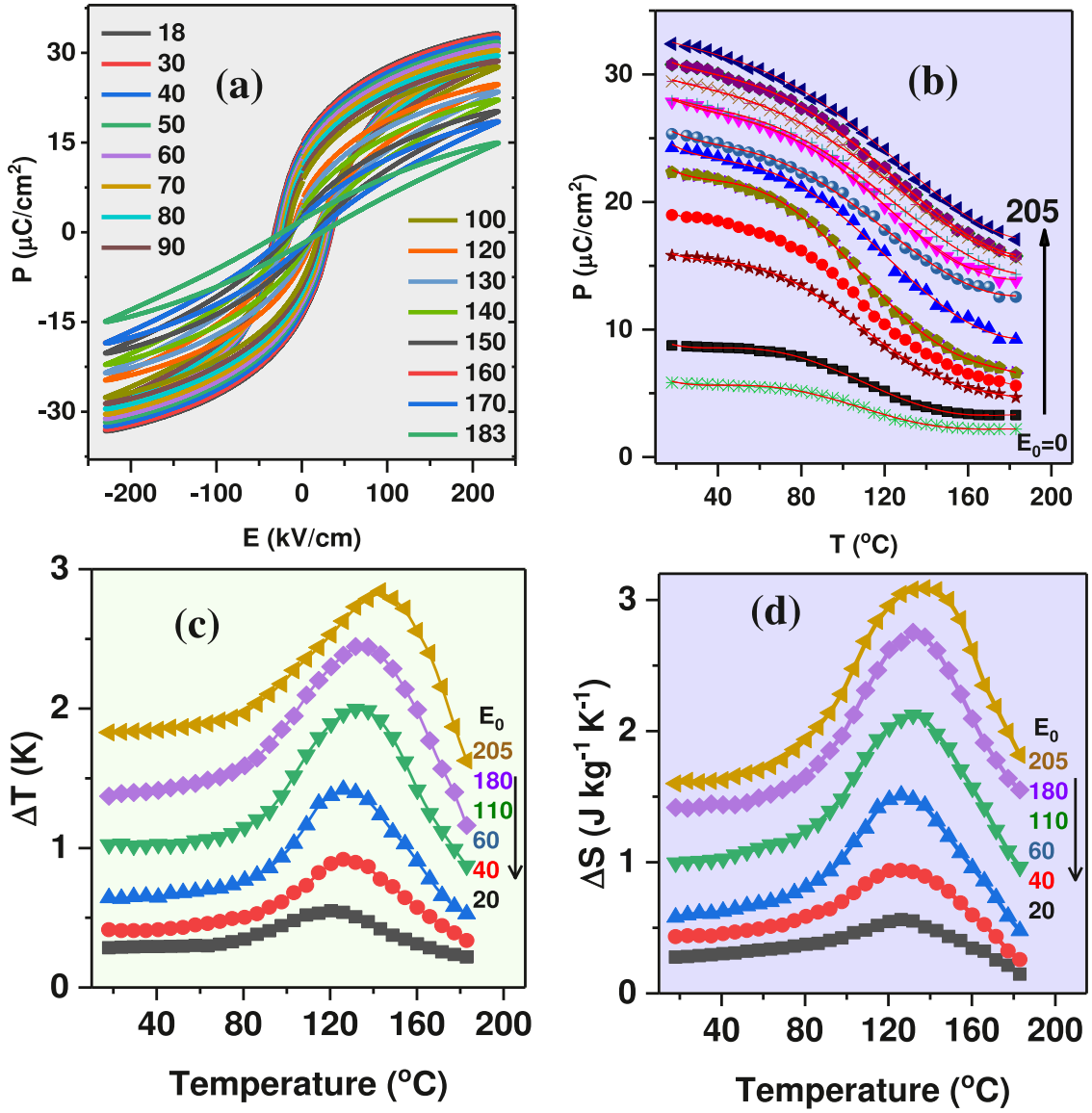

Fig. 8. P-E-T characteristics of BCZT/Pt film. (a) Polarization hysteresis loops measured at 1 kHz at fixed temperatures in the range 18–190 °C, (b) temperature evolution of polarization at different electric fields, (c) adiabatic temperature change and (d) isothermal entropy changed at fixed electric fields.

With the increase in temperature P-E loops become narrower (Fig. 8a) where P_r, P_m, and E_C values display continuous reduction, more significantly above 80 °C. The *T vs. P* relation (Fig. 8b) exhibits a clear change in polarization by means of slope change around 120 °C for lower electric fields and the degree of curve bending seems to be weaker at higher electric fields. Thus, the increase in temperature above 80 °C initiates the disorder of ferroelectric domains, or thermal fluctuation resulting in an increased entropy change around phase transition temperature.

The noteworthy change in entropy is also associated with the higher phase transition temperature detected by permittivity which is higher compared to the bulk and this change follows the relation:

$$\theta_i = \frac{\theta - 4\epsilon_0 C(\Delta\alpha)T'[Q_{12}/(s_{11}+s_{12})]}{1 - 4\epsilon_0 C(\Delta\alpha)[Q_{12}/(s_{11}+s_{12})]}$$

Here, θ_i is the effective change in phase transition temperature of the film, θ is the Curie-Weiss temperature of BCZT bulk, *C* is the Curie constant, Δα is CTE, and *Q*'s are elements of the electrostrictive tensor under constant stress and *s* are elements of elastic compliance tensor.

It can be seen that the phase transition temperature occurs at around 120 °C, relatively higher compared to the temperature of the permittivity maximum (Fig. S2). This discrepancy is the characteristic of materials with diffused phase transition as previously observed in BCZT and other ferroelectrics with a relaxor nature [15,55], which arises from the existence of random local PNRs in the paraelectric phase. The ECE parameters such as the changes in adiabatic temperature (*ΔT*) and entropy (*ΔS*) were calculated by the indirect method, using the relations based on the Maxwell thermodynamic relations $\left(\frac{\partial P}{\partial T}\right)_E = \left(\frac{\partial S}{\partial T}\right)_T$:

$$\Delta T_{ECE} = -\frac{T}{C_p \rho}\int_0^{E_{max}} \left(\frac{\partial P}{\partial T}\right)_E dE$$

$$\Delta S_{ECE} = \frac{1}{\rho}\int_0^{E_{max}} \left(\frac{\partial P}{\partial T}\right)_E dE$$

where C_p,ρ, P and E_{max} refers to the heat capacity, density of the material, polarization, and applied electric field maximum respectively. From Fig. 8(b), *P vs. T*, numerical values of pyroelectric coefficient $\left(\frac{\partial P}{\partial T}\right)$ were obtained from the seventh order polynomial fit and corresponding *ΔT* and *ΔS* were calculated. The C_p and ρ values were taken to be 0.45 J g^{-1} K^{-1} and 5.53 g/cm^3 respectively, as per the calculations from our previous study on BCZT ceramics [15].

Fig. 8(c) displays temperature-dependent *ΔT* at different electric fields in the range of 20-205 kV/cm. At any fixed electric field *ΔT* increases progressively with the temperature and presents a broad maximum around 120 °C and then shows a drop. The peak position shifts towards higher temperatures with the increase in E_0, similar to that in bulk ceramics. This feature can be attributed to the field-induced phase transition in BCZT. A similar trend can be seen in *ΔS vs. T* plot (Fig. 8d) whose maxima span over a relatively broader temperature range. The maximum ECE parameters thus were found to be $\Delta T = 2.94$ K and $\Delta S = 3.1$ J kg^{-1} K^{-1} at 205 kV/cm. These parameters are significantly larger compared to previous reports on the BCZT-family of ferroelectric ceramics. ECE parameters of various BTO-based ceramics and thick films reported in the literature are enlisted in Table 1.

The magnitude of electrocaloric responsivity $\xi = \Delta T/E$ is considered to be the measure of the ECE strength of the material. The maximum value of ξ for the BCZT/Pt film at 205 kV/cm is 0.141 K mm/kV, which is comparable to that of epitaxial thin films of BCZT [24] and other BTO-based thick films. We observed that *ΔT* as well as ξ values (at room temperature or any other temperature), increase progressively with the continuous increase in the electric field, and attain saturation around E_{0max}, a trend consistent with other relaxor-like ferroelectrics. In general, for ceramics and single crystals, the*ΔT* increase is larger around phase transition. It is interesting to note that the room temperature *ΔT* value of our sample seems to be significantly enhanced, 1.9 K at 205 kV/cm, larger than tapes of Sn-containing BTO [14].

Table 1
Comparison of observed electrocaloric parameters with the reported literature.

Sample	T_m (°C)	*ΔT* (K)	*ΔE* (kV/cm)	ξ (K mm/kV)	Refs.
Ceramic/crystal					
BCZT ceramic	90	1.32	30	0.43/ 0.42*	[15]
0.45BZT-0.55BCTsingle- crystal	109	0.46	12	0.38	[19]
$Ba_{0.786}Ca_{0.214}Ti_{0.994}Zr_{0.006}$ single crystal	122	1.05	60	0.133*	[56]
BCZT ceramic (hydrothermal)	94	1.48	60	0.246	[16]
$Ba(Zr_{0.05}Ti_{0.95})O_3$ ceramic[a]	113	2.4	30	0.8*	[11]
Thin/thick film					
BCZT/Pt thick film (2.8 μm)	120	2.94	205	0.143	Our work
$Ba(Zr_{0.2}Ti_{0.8})O_3$ thick film[b] (12 μm)	80	7.0	195	0.36	[21]
Multilayers of BTO thick film (180 × 1.4 μm)[b]		1.8	176	0.102	[57]
$Ba(Zr_{0.2}Ti_{0.8})O_3$-$Ba(Sn_{0.11}Ti_{0.89})O_3$ thick film (13 μm)[b]	0	5.2	330	0.162	[23]
BCZT/LSMO/STO (100 nm)	157	13.5	1000	0.14	[24]

* Direct ECE, a-First order phase transition, b-Tape-casting

The efficiency of the present thick films for ECE cooling applications can also be assessed from the refrigerant capacity (RC), determined from the *ΔS vs. T* plot by following the relation: $RC = \int_{T_1}^{T_2} \Delta S(T)dT$. The value of RC is 249 J/kg which is almost 70% higher than that of its bulk counterpart [15,16]. The efficiency of ECE material can also be evaluated by calculating the relative cooling capacity (RCP) in addition to *ΔT*, which is a measure of the peak broadening or the temperature at which a larger ECE can be maintained (T_{span}). Larger RCP values are obtained for higher values of the full width at half maximum of the *ΔT* curves (δT_{FWHM}) which are related as $RCP = \int_{T_1}^{T_2} |\Delta T|\delta T_{FWHM}$. The calculated RCP value at E_0=205 kV/cm was 236 K^2, which is superior to its bulk counterpart, on account of the larger T_{Span} (81 K) of BCZT thick film. The observation of higher *ΔT* with peak broadening is not satisfied in ceramics. Recently, higher *ΔT* (at 60 °C) of 2.59 K and $T_{span} = 60$ K were reported for $Na_{0.5}Bi_{0.5}TiO_3$-$Sr_{0.85}Bi_{0.10}TiO_3$ multilayer stacked structures with relaxor character [58] and T_{span}= 65 K for KNN-based multilayers. These studies demonstrate that better composition and microstructural control during the growth processes enable larger breakdown fields for greater caloric performance. The present results of thick films with distorted unit cell compared to the bulk, due to lower

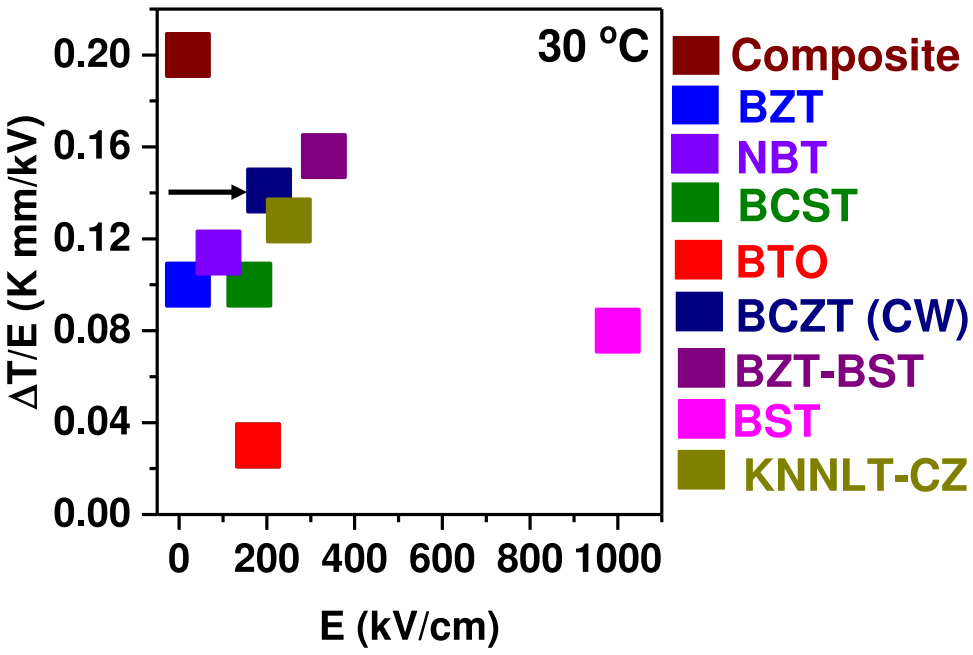

Fig. 9. Comparison of room temperature ECE potential observed for lead-free thick films at their respective maximum electric fields related to the current work (CW, marked with arrow). The materials reported in literature are BTO [57], $Ba(Zr_{0.2}Ti_{0.8})O_3$ (BZT) [59], $Ba_{0.8}Sr_{0.2}TiO_3$ (BST) [60], $Na_{0.5}Bi_{0.5}TiO_3$ (NBT) [61], $(K_{0.49}Na_{0.49}Li_{0.02})(Nb_{0.8}Ta_{0.2})O_3$-$CaZrO_3$ (KNLNT - CZ) [22], $(Ba_{0.95}Ca_{0.05})$-$(Ti_{0.94}Sn_{0.06})O_3$ (BCST) [14], $Ba(Zr_{0.2}Ti_{0.8})O_3$−$Ba(Sn_{0.11}Ti_{0.89})O_3$ (BZT-BST) [23], laminate composite of $BaTi_{0.89}Sn_{0.11}O_3$/$BaTi_{0.85}Zr_{0.15}O_3$/ $BaTi_{0.89}Hf_{0.11}O_3$ [62].

lattice-mismatched Pt, are of greater advantage in view of practical applications. The observation of moderate polarization, lower loss, and higher T_{span} illustrate the fact that BCZT/Pt films have superior properties compared to their bulk counterparts. Through the cost-effective deposition of thick films with EPD followed by laser annealing one can find the tuning between the growth process and the quality of thick films. This method can be considered as an alternative for flexible thick film structures for the integration of ferroelectrics with metals for future caloric applications under electric fields.

4. Conclusions

High-quality thick films of BCZT on flexible Pt foil were obtained by the combination of EPD and laser annealing at an optimized energy density. The resulting film exhibited a clear coexistence of rhombohedral, orthorhombic, and tetragonal phases, a characteristic of BCZT at MPB. A uniform grain morphology that is similar to the bulk nature (micrometre-sized grains) was observed in the annealed films. Electron probe microanalysis was used to determine the chemical composition of the film, which was consistent with the expected cationic ratios. Hysteresis loops under higher electric fields demonstrated saturation characteristics with $P_r = 14\ \mu C/cm^2$, $P_S = 38\ \mu C/cm^2$, and $E_C = 13.5$ kV/cm, considered to be significantly "softer" compared to nano-granular thin films. Dynamic hysteresis scaling was investigated from the polarization behavior at different E_0 and f that follows relation $< A> \propto f^{-0.07}E^{1.7}$ in the sub-saturation region and $< A> \propto f^{-0.04}E^{1.1}$ in the saturated regions. The lower exponent value of frequency indicates that the domain reversal consumes less energy than classical BTO at higher electric fields. Marked improvement of energy storage density of 7.3 J/cm^3 compared to the high-density ceramic samples was observed. From the ECE studies improved parameters such as $\Delta T = 2.94$ K at the phase transition temperature and a higher T_{span} of 81 K were observed which translates to larger RCP = 236 K^2 and RC = 249 J/kg.

CRediT authorship contribution statement

E. Venkata Ramana: Conceptualization, Methodology, Data curation, Writing – original draft, Investigation. **N.V. Prasad:** Investigation. **N.M. Ferreira:** Investigation. **A. Mahajan:** Investigation. **I. Bdikin:** Investigation. **M.A. Valente:** Funding acquisition, Writing – review & editing. **Fadl A. Essa:** Investigation. **B. Saleh:** Investigation.

Declaration of Competing Interest

The authors declare that they have no known competing financial interests or personal relationships that could have appeared to influence the work reported in this paper.

Data Availability

Data will be made available on request.

Acknowledgment

This work was developed within the scope of the project 032-88-ARH/2018 (EVR) financed by national funds (OE) through the Portuguese foundation for science and technology (FCT), in the scope of the framework contract foreseen in the numbers 4, 5 and 6 of the article 23, of the Decree-Law 57/2016, of August 29, changed by Law 57/2017, of July 19. The authors also acknowledge financial I3N, UIDB/ 50025/ 2020 & UIDP/50025/2020 funded by FCT/MEC. IB wishes to acknowledge FCT for financial support: IF/00582/2015. This study is financed by Taif University Researchers Supporting Project number (TURSP-2020/49), Taif University, Taif, Saudi Arabia. The author (BS) would like to thank Taif University for its financial support.

Supplementary materials

Supplementary material associated with this article can be found, in the online version, at doi:10.1016/j.surfin.2022.102257.

References

[1] T. Zheng, J. Wu, D. Xiao, J. Zhu, Recent development in lead-free perovskite piezoelectric bulk materials, Prog. Mater. Sci. 98 (2018) 552–624.
[2] Y. Saito, H. Takao, T. Tani, T. Nonoyama, K. Takatori, T. Homma, T. Nagaya, M. Nakamura, Lead-free piezoceramics, Nature 432 (2004) 84–87.
[3] J. Wu, Perovskite lead-free piezoelectric ceramics, J. Appl. Phys. 127 (2020), 190901.

[4] L.F. Zhu, B.P. Zhang, L. Zhao, S. Li, Y. Zhou, X.-C. Shi, N. Wang, Large piezoelectric effect of (Ba,Ca)TiO_3–x$Ba(Sn,Ti)O_3$ lead-free ceramics, J. Eur. Ceram. Soc. 36 (2016) 1017–1024.

[5] W. Liu, X. Ren, Large piezoelectric effect in Pb-free ceramics, Phys. Rev. Lett. 103 (2009), 257602.

[6] H. Guo, B.K. Voas, S. Zhang, C. Zhou, X. Ren, S.P. Beckman, X. Tan, Polarization alignment, phase transition, and piezoelectricity development in polycrystalline $0.5Ba(Zr_{0.2}Ti_{0.8})O_3$-$0.5(Ba_{0.7}Ca_{0.3})TiO_3$, Phys. Rev. B 90 (2014), 014103.

[7] Z. Kutnjak, B. Rožič, R. Pirc, Electrocaloric Effect: Theory, Measurements, and Applications, Wiley Encyclopedia of Electrical and Electronics Engineering, John Wiley & Sons, Hoboken, NJ, USA, 2015, pp. 1–19.

[8] F. Zhuo, Q. Li, J. Gao, Y. Ji, Q. Yan, Y. Zhang, H.-H. Wu, X.-Q. Xi, X. Chu, W. Cao, Giant negative electrocaloric effect in $(Pb,La)(Zr,Sn,Ti)O_3$ antiferroelectrics near room temperature, ACS Appl. Mater. Interfaces 10 (2018) 11747–11755.

[9] A.S. Mischenko, Q. Zhang, J.F. Scott, R.W. Whatmore, N.D. Mathur, Giant electrocaloric effect in thin-film $PbZr_{0.95}Ti_{0.05}O_3$, Science 311 (2006) 1270–1271.

[10] U. Plaznik, A. Kitanovski, B. Rožič, B. Malič, H. Uršič, S. Drnovšek, J. Cilenšek, M. Vrabelj, A. Poredoš, Z. Kutnjak, Bulk relaxor ferroelectric ceramics as a working body for an electrocaloric cooling device, Appl. Phys. Lett. 106 (2015), 043903.

[11] X.D. Jian, B. Lu, D.D. Li, Y.B. Yao, T. Tao, B. Liang, J.H. Guo, Y.J. Zeng, J.L. Chen, S.G. Lu, Direct measurement of large electrocaloric effect in $Ba(Zr_xTi_{1-x})O_3$ ceramics, ACS Appl. Mater. Interfaces 10 (2018) 4801–4807.

[12] C.L. Zhao, J.L. Yang, Y.L. Huang, X.H. Hao, J.G. Wu, Broad-temperature-span and large electrocaloric effect in lead-free ceramics utilizing successive and metastable phase transitions, J. Mater. Chem. A 7 (2019) 25526–25536.

[13] M.D. Li, X.G. Tang, S.M. Zeng, Q.X. Liu, Y.P. Jiang, T.F. Zhang, W.H. Li, Large electrocaloric effect in lead-free $Ba(Hf_xTi_{1-x})O_3$ ferroelectric ceramics for clean energy applications, ACS Sustain. Chem. Eng. 6 (2018) 8920–8925.

[14] H. Du, Y. Chang, C. Li, Q. Hu, J. Pang, Y. Sun, F. Weyland, N. Novak, L. Jin, Ultrahigh room temperature electrocaloric response in lead-free bulk ceramics via tape casting, J. Mater. Chem. C 7 (2019) 6860–6866.

[15] E.V. Ramana, N.M. Ferreira, A. Mahajan, D.M. Tobaldi, I. Bdikin, B. Rožič, Z. Kutnjak, M.A. Valente, Processing mediated enhancement of ferroelectric and electrocaloric properties in $Ba(Ti_{0.8}Zr_{0.2})O_3$–$(Ba_{0.7}Ca_{0.3})TiO_3$ lead-free piezoelectrics, J. Eur. Ceram. Soc. 41 (2021) 6424–6440.

[16] Z. Hanani, S. Merselmiz, D. Mezzane, M.B. Amjoud, A. Bradeško, B. Rožič, M. Lahcini, M. El Marssi, A.V. Ragulya, I.A. Luk'yanchuk, Z. Kutnjak, M. Gouné, Thermally-stable high energy storage performances and large electrocaloric effect over a broad temperature span in lead-free BCZT ceramic, RSC Adv. 10 (2020) 30746–30755.

[17] Z. Hanani, D. Mezzane, M.b. Amjoud, A.G. Razumnaya, S. Fourcade, Y. Gagou, K. Hoummada, M. El Marssi, M. Gouné, Phase transitions, energy storage performances and electrocaloric effect of the lead-free $Ba_{0.85}Ca_{0.15}Zr_{0.10}Ti_{0.90}O_3$ ceramic relaxor, J. Mater. Sci. Mater. Electron. 30 (2019) 6430–6438.

[18] S. Merselmiz, Z. Hanani, S. Ben Moumen, A. Matavž, D. Mezzane, N. Novak, Z. Abkhar, L. Hajji, M.b. Amjoud, Y. Gagou, K. Hoummada, D. Črešnar, Z. Kutnjak, B. Rožič, Enhanced electrical properties and large electrocaloric effect in lead-free Ba0.8Ca0.2ZrxTi1−xO3 (x = 0 and 0.02) ceramics, J. Mater. Sci. Mater. Electron. 31 (2020) 17018–17028.

[19] G. Singh, I. Bhaumik, S. Ganesamoorthy, R. Bhatt, A.K. Karnal, V.S. Tiwari, P. K. Gupta, Electro-caloric effect in $0.45BaZr_{0.2}Ti_{0.8}O_3$-$0.55Ba_{0.7}Ca_{0.3}TiO_3$ single crystal, Appl. Phys. Lett. 102 (2013), 082902.

[20] M. Sanlialp, V.V. Shvartsman, M. Acosta, B. Dkhil, D.C. Lupascu, Strong electrocaloric effect in lead-free $0.65Ba(Z_{r0.2}Ti_{0.8})O_3$-$0.35(Ba_{0.7}Ca_{0.3})TiO_3$ ceramics obtained by direct measurements, Appl. Phys. Lett. 106 (2015), 062901.

[21] H.J. Ye, X.S. Qian, D.Y. Jeong, S. Zhang, Y. Zhou, W.Z. Shao, L. Zhen, Q.M. Zhang, Giant electrocaloric effect in $BaZr_{0.2}Ti_{0.8}O_3$ thick film, Appl. Phys. Lett. 105 (2014), 152908.

[22] Y. Zhao, J. Du, J. Yang, L. Zhu, Y. Wang, Y. Li, X. Hao, Large room-temperature electrocaloric response realized in potassium-sodium niobate by a relaxor enhancement effect and multilayer ceramic construct, ACS Appl. Mater. Interfaces 14 (2022) 11626–11635.

[23] J. Li, Y. Chang, S. Yang, Y. Tian, Q. Hu, Y. Zhuang, Z. Xu, F. Li, Lead-free bilayer thick films with giant electrocaloric effect near room temperature, ACS Appl. Mater. Interfaces 11 (2019) 23346–23352.

[24] A. Barman, S. Chatterjee, C. Ou, Y.Y. Tse, N. Banerjee, S. Kar-Narayan, A. Datta, D. Mukherjee, Large electrocaloric effect in lead-free ferroelectric $Ba_{0.85}Ca_{0.15}Ti_{0.9}Zr_{0.1}O_3$ thin film heterostructure, APL Mater. 9 (2021), 021115.

[25] B. Giera, L.A. Zepeda-Ruiz, A.J. Pascall, T.H. Weisgraber, Mesoscale particle-based model of electrophoretic deposition, Langmuir 33 (2017) 652–661.

[26] E.V. Ramana, N.M. Ferreira, A. Mahajan, M.C. Ferro, F. Figueiras, M.P.F. Graça, M. A. Valente, Effect of laser processing on physical properties of $(Ba_{0.85}Ca_{0.15}Ti_{0.9}Zr_{0.1}O_3)$ lead-free thick films fabricated by the electrophoretic deposition, J. Phys. Chem. Solids 113 (2018) 94–101.

[27] E.V. Ramana, A. Mahajan, M.P.F. Graça, S.K. Mendiratta, J.M. Monteiro, M. A. Valente, Structure and ferroelectric studies of $(Ba_{0.85}Ca_{0.15})(Ti_{0.9}Zr_{0.1})O_3$ piezoelectric ceramics, Mater. Res. Bull. 48 (2013) 4395.

[28] E.V. Ramana, N.M. Ferreira, M.P.F. Graça, M.A. Valente, Effect of processing parameters on ferroelectric properties of $0.5(Ba,Ca)TiO_3$-$0.5Ba(Zr,Ti)O_3$: bulk, thin films and fibers, Ferroelectrics 466 (2014) 36–41.

[29] Microanalysis consultants limited, UK. https://www.micro-analysis.com/standards/universal/55-standard.asp.

[30] K. Brajesh, K. Tanwar, M. Abebe, R. Ranjan, Relaxor ferroelectricity and electric-field-driven structural transformation in the giant lead-free piezoelectric (Ba,Ca)(Ti,Zr)O_3, Phys. Rev. B 92 (2015), 224112.

[31] J. Xing, M. Radovic, A. Muliana, Thermal properties of $BaTiO_3$/Ag composites at different temperatures, Compos. B Eng. 90 (2016) 287–301.

[32] T. Kim, J.N. Hanson, A. Gruverman, A.I. Kingon, S.K. Streiffer, Ferroelectric behavior in nominally relaxor lead lanthanum zirconate titanate thin films prepared by chemical solution deposition on copper foil, Appl. Phys. Lett. 88 (2006), 262907.

[33] S. Baba, J. Akedo, Fiber laser annealing of nanocrystalline PZT thick film prepared by aerosol deposition, Appl. Surf. Sci. 255 (2009) 9791–9795.

[34] G. Catalan, B. Noheda, J. McAneney, L.J. Sinnamon, J.M. Gregg, Strain gradients in epitaxial ferroelectrics, Phys. Rev. B 72 (2005), 020102.

[35] A. Lisińska-Czekaj, D. Czekaj, Study of the layer-type BST thin film with X-ray diffraction and X-ray photoelectron spectroscopy, Materials 15 (2022) 578.

[36] E.V. Ramana, J. Zavašnik, M.P.F. Graça, M.A. Valente, Magnetoelectric studies on $CoFe_2O_4$/$0.5(BaTi_{0.8}Zr_{0.2}O_3)$-$0.5(Ba_{0.7}Ca_{0.3}TiO_3)$ lead-free bilayer thin films derived by the chemical solution deposition, J. Appl. Phys. 120 (2016), 074108.

[37] A. Piorra, V. Hrkac, N. Wolff, C. Zamponi, V. Duppel, J. Hadermann, L. Kienle, E. Quandt, $(Ba_{0.85}Ca_{0.15})(Ti_{0.9}Zr_{0.1})O_3$ thin films prepared by PLD: relaxor properties and complex microstructure, J. Appl. Phys. 125 (2019), 244103.

[38] C. Bhardwaj, B.S.S. Daniel, D. Kaur, Pulsed laser deposition and characterization of highly tunable $(1-x)Ba(Zr_{0.2}Ti_{0.8})O_3$–$x(Ba_{0.7}Ca_{0.3})TiO_3$ thin films grown on $LaNiO_3$/Si substrate, J. Phys. Chem. Solids 74 (2013) 94–100.

[39] Z. Feng, D. Shi, S. Dou, X. Tang, Y. Hu, Large piezoelectric effect in lead-free $Ba(Zr_{0.2}Ti_{0.8})O_3$–$(Ba_{0.7}Ca_{0.3})TiO_3$ films prepared by screen printing with solution infiltration process, Thin Solid Films 527 (2013) 110–113.

[40] S. Abhinay, R. Mazumder, A. Seal, A. Sen, Tape casting and electrical characterization of $0.5Ba(Zr_{0.2}Ti_{0.8})O_3$–$0.5(Ba_{0.7}Ca_{0.3})TiO_3$ (BZT–0.5BCT) piezoelectric substrate, J. Eur. Ceram. Soc. 36 (2016) 3125–3137.

[41] S. Gupta, S. Priya, Ferroelectric properties and dynamic scaling of ⟨100⟩ oriented $(K_{0.5}Na_{0.5})NbO_3$ single crystals, Appl. Phys. Lett. 98 (2011), 242906.

[42] C.-M. Wang, K. Lau, Q. Wang, Dynamic hysteresis and scaling behaviours of lead-free $0.94Bi_{0.5}Na_{0.5}TiO_3$-$0.06BaTiO_3$ bulk ceramics, RSC Adv. 6 (2016) 30148–30153.

[43] F. Li, S. Zhang, T. Yang, Z. Xu, N. Zhang, G. Liu, J. Wang, J. Wang, Z. Cheng, Z. G. Ye, J. Luo, T.R. Shrout, L.Q. Chen, The origin of ultrahigh piezoelectricity in relaxor-ferroelectric solid solution crystals, Nat. Commun. 7 (2016) 13807.

[44] Y. Zhang, B. Long, Y. Wen, Z. Zhang, W. Cao, Electric field and frequency dependent scaling behavior of dynamic hysteresis in relaxor-based ferroelectric $0.71Pb(Mg_{1/3}Nb_{2/3})O_3$–$0.29PbTiO_3$ single crystal, J. Alloy. Compd. 775 (2019) 435–440.

[45] X. Xia, C. Li, J. Zeng, L. Zheng, G. Li, Scaling behavior of dynamic hysteresis of PMN-PT relaxor ferroelectric ceramics near the morphotropic phase boundary, J. Am. Ceram. Soc. 103 (2020) 2694–2701.

[46] N. Wongdamnern, K. Kanchiang, A. Ngamjarurojana, S. Ananta, Y. Laosiritaworn, A. Charoenphakdee, S. Gupta, S. Priya, R. Yimnirun, Crystal-structure dependent domain-switching behavior in $BaTiO_3$ ceramic, Smart Mater. Struct. 23 (2014), 085022.

[47] P. Peng, H. Nie, Z. Liu, G. Wang, X. Dong, Y. Zhang, C. Duan, X. Tang, Scaling behavior for $(Bi_{0.5}Na_{0.5})TiO_3$ based lead-free relaxor ferroelectric ceramics, J. Appl. Phys. 122 (2017), 064102.

[48] S.R. Reddy, V.V.B. Prasad, S. Bysakh, V. Shanker, N. Hebalkar, S.K. Roy, Superior energy storage performance and fatigue resistance in ferroelectric BCZT thin films grown in an oxygen-rich atmosphere, J. Mater. Chem. C 7 (2019) 7073–7082.

[49] J. Li, F. Li, Z. Xu, S. Zhang, Multilayer lead-free ceramic capacitors with ultrahigh energy density and efficiency, Adv. Mater. 30 (2018), 1802155.

[50] K. Wu, H. Wang, X. Zhou, L. Yang, B. Yu, Q. Yang, Q. Zheng, D. Lin, Large energy storage density and efficiency of Sm_2O_3-doped $Ba_{0.85}Ca_{0.15}Zr_{0.08}Ti_{0.92}O_3$ lead-free ceramics, J. Mater. Sci. Mater. Electron. 32 (2021) 9650–9660.

[51] V.S. Puli, D.K. Pradhan, D.B. Chrisey, M. Tomozawa, G.L. Sharma, J.F. Scott, R. S. Katiyar, Structure, dielectric, ferroelectric, and energy density properties of (1 − x)BZT–xBCT ceramic capacitors for energy storage applications, J. Mater. Sci. 48 (2013) 2151–2157.

[52] M.A. Rafiq, A. Maqbool, I.H. Khan, M.U. Manzoor, A. Shuaib, A.S. Hakeem, A facile and cost-effective approach for the fabrication $Bi_{0.5}Na_{0.5}TiO_3$ thick films on flexible substrate for energy storage capacitor applications, Ceram. Int. 46 (2020) 25113–25121.

[53] P. Maksymovych, N. Balke, S. Jesse, M. Huijben, R. Ramesh, A.P. Baddorf, S. V. Kalinin, Defect-induced asymmetry of local hysteresis loops on $BiFeO_3$ surfaces, J. Mater. Sci. 44 (2009) 5095–5101.

[54] P. Maksymovych, S. Jesse, M. Huijben, R. Ramesh, A. Morozovska, S. Choudhury, L.Q. Chen, A.P. Baddorf, S.V. Kalinin, Intrinsic nucleation mechanism and disorder effects in polarization switching on ferroelectric surfaces, Phys. Rev. Lett. 102 (2009), 017601.

[55] E.V. Ramana, V.V. Kiran, T.B. Sankaram, Dielectric and pyroelectric properties of Sr-modified $(Na_{0.5}Bi_{0.5})Bi_4Ti_4O_{15}$ ceramics, J. Alloy. Compd. 456 (2008) 271–276.

[56] D. Liu, Q. Li, Q. Yan, Electro-caloric effect in a BCZT single crystal, Cryst. Eng. Comm. 20 (2018) 1597–1602.

[57] Y. Bai, G. Zheng, S. Shi, Direct measurement of giant electrocaloric effect in $BaTiO_3$ multilayer thick film structure beyond theoretical prediction, Appl. Phys. Lett. 96 (2010), 192902.

[58] L. Zhu, X. Meng, J. Zhu, Y. Zhao, Y. Li, X. Hao, Enhanced room temperature electrocaloric effect in lead-free relaxor ferroelectric NBT ceramics with excellent temperature stability, J. Alloy. Compd. 892 (2022), 162241.

[59] C. Molin, P. Neumeister, H. Neubert, S.E. Gebhardt, Multilayer ceramics for electrocaloric cooling applications, Energy Technol. 6 (2018) 1543–1552.

[60] R. Su, D. Zhang, Y. Liu, J. Lu, Z. Wang, L. Li, J. Bian, M. Wu, X. Lou, Y. Yang, Novel lead-free ferroelectric film by ultra-small $Ba_{0.8}Sr_{0.2}TiO_3$ nanocubes assembled for a large electrocaloric effect, Phys. Chem. Chem. Phys. 18 (2016) 29033–29040.

[61] F. Le Goupil, A. Baker, F. Tonus, A. Berenov, C.A. Randall, N.M. Alford, Direct measurement of electrocaloric effect in lead-free $(Na_{0.5}Bi_{0.5})TiO_3$-based multilayer ceramic capacitors, J. Eur. Ceram. Soc. 39 (2019) 3315–3319.

[62] R.W. Yin, J.J. Li, X.P. Su, S.Q. Qin, C.Y. Yu, Y.X. Hou, C.B. Liu, Y.J. Su, L.J. Qiao, T. Lookman, Y. Bai, Emergent enhanced electrocaloric effect within wide temperature span in laminated composite ceramics, Adv. Funct. Mater. 32 (2022), 2108182.